Analytical Model of Torque-Prediction for a Novel Hybrid Rotor Permanent Magnet Machines

YU-XI LIU [1,2], **LI-YI LI** [1], **(Senior Member, IEEE), QIN-HE GAO** [2], **JI-WEI CAO** [1],
REN-HAO WANG [1], **AND ZHI-YIN SUN** [1], **(Member, IEEE)**

[1]Department of Electrical Engineering, Harbin Institute of Technology, Harbin 150001, China
[2]Department of Armament Science and Technology, Xi'an High-tech Institution, Xi'an 710025, China

Corresponding author: Ji-Wei Cao (caojiwei@hit.edu.cn)

ABSTRACT This paper presents an analytical method for predicting the electromagnetic performance in permanent magnet (PM) machine with the spoke-type rotor (STR) and a proposed hybrid rotor structure (HRS), respectively. The key of this method is to combine magnetic field analysis model (MFAM) with the magnetic equivalent circuit model. The influence of the irregular PM shape is considered by the segmentation calculation. To obtain the boundary condition in the MFAM, respectively, two equivalent methods on the rotor side are proposed. In the STR, the average flux density of the rotor core outer-surface is calculated to solve the Laplace's equation with considering for the rotor core outer-surface eccentric. In the HRS, based on the Thevenin's theorem, the equivalent parameters of PM remanence B_{reB} and thickness h_{pme} are obtained as a given condition, which can be utilized to compute the air-gap flux density by conventional classic magnetic field analysis model of surface-mounted PMs with air-gap region. Finally, the proposed analytical models are verified by the finite element analysis (FEA) with comparisons of the air-gap flux density, flux linkage, back-EMF and electromagnetic torque, respectively. Furthermore, the performance that the machine with the proposed hybrid structure rotor can improve the torque density as explained.

INDEX TERMS Analytical method, hybrid PM rotor structure, rotor core outer-surface eccentric, magnetic equivalent circuit model (MECM).

I. INTRODUCTION

Recently, interior permanent magnet synchronous machine (IPMSM) has been widely applied to the electric vehicles (EVs) field and aerospace industry all over the world, in view of the excellent performances of high-power density, high efficiency, and high reliability [1]–[5]. To further improve the torque density, the spoke-type PM machines has been adopted due to the advantage of the flux concentrated structure [6]–[8]. In some applications, such as high dynamic response machine with low moment of inertia, rotor outer diameter is strictly restricted. Therefore, the spoke-type IPMSMs are significantly effective because it can increase magnetic flux area of IPMSMs from the larger magnet surface area compared with other types, which means that the larger

The associate editor coordinating the review of this manuscript and approving it for publication was Bora Onat.

torque can be obtained [9]–[11]. Moreover, consequent-Pole and Hybrid-Pole PM Machines are adopted to improve the output torque and efficiency. Then, the flux barriers are employed to improve the magnetic symmetry and reduce the saturation of the stator yoke [12]. Two novel consequent-pole PM machines with different pole sequences are adopted. In order to provide assistant flux and suppress the subharmonics, the tangential PMs are embedded into the rotors to form the novel hybrid-pole PM machines [13].

The analytical methods can offer computation speed and flexibility at the initial design and optimization process [14], [15]. There are many related research literatures on magnetic field analysis, such as conventional scalar magnetic field analysis [16], [17] and subdomain magnetic field analysis [18]–[20]. However, in many situations, the boundary conditions are not ideal that the geometric model is irregular, which is result in inaccurate prediction of electromagnetic

performances compared with the FEA. In order to map the spoke PMs in polar coordinates, the rectangular geometry with rectangular spoke PMs assisted by hub magnets is approximated by a combination of arc shaped subdomains [21]. To match the standard boundary conditions of the Poisson and Laplace equations, the trapezoid magnet is simplified to sector magnets, the dimension of the sector magnet is calculated with a lumped magnetic circuit model [7]. In [22], it presents an improved analytical method for the surface mounted PM machines accounting for any eccentric rotor shape by the equivalent surface current of magnet pole. Meanwhile, taking into account the saturation and nonlinearity of magnetic material, the magnetic bridges are equivalent to fan-shaped saturation regions [23], [24]. For getting standard boundary conditions, a lumped parameter magnetic circuit model and iterative method are employed to calculate the permeability [25]–[27]. However, it's hard to generalize because of the rotor structure with different shape and various PM arrangements forms.

This paper presents an analytical method for the PM machine with non-ideal regular shape rotor structure, which considers the rotor core outer-surface eccentric and the proposed hybrid rotor structure, respectively. The proposed analytical model takes advantage of the characteristics of magnetic field analysis model and the magnetic equivalent circuit model. The corresponding boundary condition in the STR and the equivalent parameters in the HRS are obtained by the MECM, respectively. The predicted accuracy of the proposed two analytical models is validated by FEA. Moreover, the proposed hybrid rotor structure can improve torque density due to increasing the magnetic flux area of IPMSMs and the equivalent thickness of the PM. In Section II, the topology structure of the studied machine will be given. In Section III, the equivalent magnetic circuit model of rotor will be presented to obtain the boundary conditions and equivalent parameters. In Section IV, model of the air-gap magnetic field analysis in the STR and HRS are built. In Section V, analytical prediction accuracy will be verified by FEA. Finally, the conclusions will be derived in Section VI.

II. TOPOLOGIES AND FEATURES

The cross section of the hybrid PMSM with the Spoke-Type and surface-mounted PMs is shown in Fig 1. A 10-pole/12slot motor as the studied model is adopted to highlight the advantage of analytical method. For the sake of simplification, the stator is assumed to be infinitely permeable. It is assumed that the permeability of all materials in machine is isotropic and homogenous. The effects of the axial end and eddy current in the magnetic material are neglected [28].

The embedded PMs are tangentially magnetized and surface-mounted PMs are parallel magnetized with a linear demagnetization characteristic, respectively.

The main design parameters of the Spoke-Type rotor (model A) and hybrid rotor structure (model B) IPMSM are listed in Table 1:
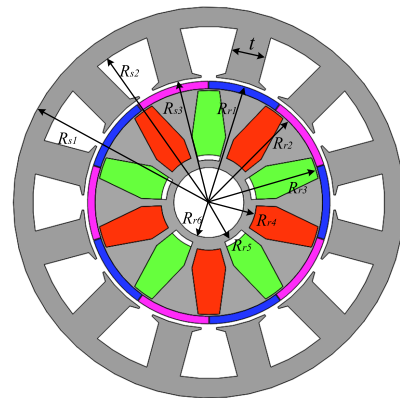
FIGURE 1. Initial machine model of 10-pole/12slot with hybrid structure rotor.

TABLE 1. Main PM machine parameters.

Symbol	Quantity	Value and unit
p	Number of pole-pairs	5
Q_s	Number of stator slots	12
ω_r	Rated speed	1500rpm
I_r	Rated current	25A
B_r	Magnet remanence	0.4T
L_{ef}	Armature effective length	100mm
R_{s1}	Radius of the stator outer surface	39mm
R_{s3}	Radius of the stator inner surface	25mm
N	Number of turns per phase	48
t	Tooth width	6.9mm
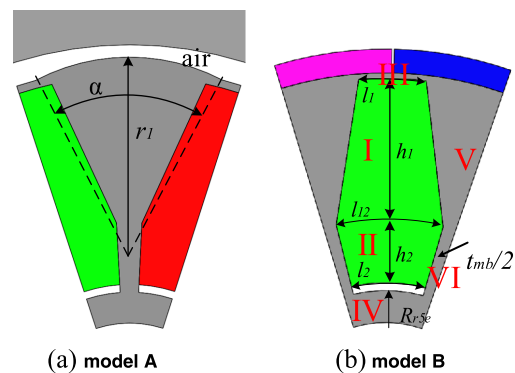
FIGURE 2. Model of the rotor structure (a) the rotor core outer-surface eccentric (b) hybrid PM rotor structure.

Partial enlarged views of two rotor structures are shown as Fig 2. In order to highlight the details in the STR, the core is placed in the symmetrical center of model A. It is worth noting that the model B is similar to the model A when the thickness of the surface-mounted PM in the hybrid rotor structure is close to 0 mm. In order to reduce the harmonic content of the air-gap magnetic density, the eccentric structure is often adopted on the outer surface of the rotor core.

III. ROTOR MAGNETIC CIRCUIT MODEL

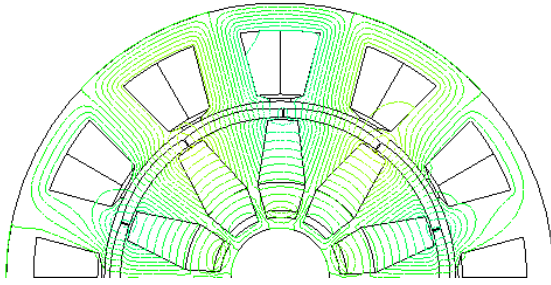Due to the non-idealization of the rotor structure arrangement, the EMCM is calculated to obtain the rotor flux to

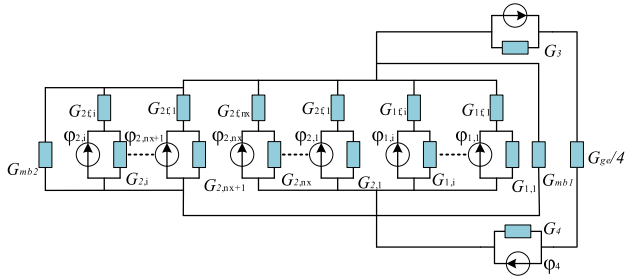**FIGURE 3.** The Motor no-load magnetic line distribution.

FIGURE 4. The equivalent magnetic circuit model.

air gap. For two rotor pole structures, the no-load air-gap magnetic density can be calculated by the Poisson's equation with the air-gap boundary condition in model A, and conventional classic magnetic field analysis model of equivalent surface-mounted PMs parameters with air gap in model B, respectively.

Because the magnetic circuit structures of the two models are very similar, the presented EMCM is compatible with both rotor pole structures as shown in Fig 3.

As shown in Fig 2, Fig 3 and Fig 4, it is obvious that the flux by the Spoke-Type PMs generated can be divided three parts: the main flux through the airgap, eventually, the leakage flux through the magnetic bridge of PMs top and rotor yoke, respectively. The Spoke-Type PMs is composed of two inverted trapezoids magnet, it can be replaced by n_1 and n_2 sector magnets in parallel. h_1 and h_2 are height of two inverted trapezoids magnets. l_1, l_{12}, l_2 are the widths of trapezoids, respectively. t_{mb} is the magnetic bridge width between both PMs in the VI region.

The magnet flux source $\varphi_{1,i}$, $\varphi_{2,i}$ and the magnetic permeance $G_{1,i}$, $G_{2,i}$ of the ith magnet piece in I and II regions, respectively, can be expressed by:

$$\varphi_{1,i} = B_r \Delta h_1 L_{ef} \tag{1}$$

$$\varphi_{2,i} = B_r \Delta h_2 L_{ef} \tag{2}$$

$$G_{1,i} = \frac{\mu_0 \mu_{rm} \Delta h_1 L_{ef}}{\Delta l_{1,i}} \tag{3}$$

$$G_{2,i} = \frac{\mu_0 \mu_{rm} \Delta h_2 L_{ef}}{\Delta l_{2,i}} \tag{4}$$

where B_r is the magnet remanence, L_{ef} is the effective length of rotor and stator, μ_0 is the permeability of the vacuum, μ_{rm}

is the magnet relative permeability; and

$$\Delta h_1 = \frac{h_1}{n_1} \quad \Delta h_2 = \frac{h_2}{n_2} \tag{5}$$

$$\Delta l_{1,i} = l_1 + \frac{(l_{12} - l_1)(i-1)}{n_1} \quad \Delta l_{2,i} = l_2 + \frac{(l_{12} - l_2)(i-1)}{n_2} \tag{6}$$

The magnet flux source φ_3 and the magnetic permeances G_3 and G_4 of the surface-mounted PMs, respectively, when considering slot less stator and the polar arc coefficient is 1, can be calculated by:

$$\varphi_3 = \frac{\pi(R_{r2} + R_{r1})}{4p} L_{ef} B_r \tag{7}$$

$$G_3 = G_4 = \mu_0 \mu_{rm} \frac{\pi(R_{r1} + R_{r2})}{4p(R_{r1} - R_{r2})} L_{ef} \tag{8}$$

where p is the number of pole pairs, R_{r1} and R_{r2} is the radius of the rotor outer surface and rotor core, respectively.

The magnetic permeance G_{ge} of air-gap can be calculated by:

$$G_{ge} = \mu_0 \frac{\pi(R_{s3} + R_{r1})}{2p(R_{s3} - R_{r1})} L_{ef} \tag{9}$$

where R_{s3} is the radius of the stator bore.

The flux density in magnetic bridge region is at a high level of saturation on the B-H curve of the silicon steel, the relative permeability μ_{r1} and μ_{r2} can be assumed as a small constant where the flux density is 2.1T [3], [4], [29]. The leakage magnetic permeance G_{mb1}, and G_{mb2} in III and IV regions can be calculated by:

$$G_{mb1} = \frac{\mu_0 \mu_{r1}(R_{r2} - R_{r3})L_{ef}}{l_1} \tag{10}$$

$$G_{mb2} = \frac{\mu_0 \mu_{r2}(R_{r5e} - R_{r6})L_{ef}}{l_2} \tag{11}$$

where R_{r5e} is the average value of R_{r4} and R_{r5}, R_{r6} is the radius of the shaft.

The calculation method of the core magnetic permeance is the same as that of the PMs in I or II regions, it is divided into many small pieces. According to the shape of the path, n parallel computing units are divided as:

$$G_{1f,i} = \frac{\mu_0 \mu_{rf1} \Delta h_{1f} L_{ef}}{i \Delta h_1} \tag{12}$$

where

$$\Delta h_{1f} = \frac{\pi R_{r3}}{2p(n_1 + n_x)} \tag{13}$$

It is worth that the flux excited by the PMs in II region is divided into two directions: part of it is through the V region, others are through the IV region and the VI region as shown in Fig 3. The magnetic permeance $G_{2f,i}$ of the rotor core, where the magnetic flux generated by the PMs in II region
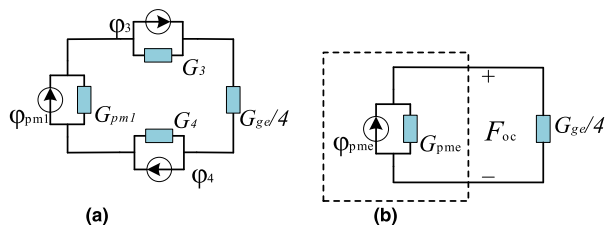
FIGURE 5. Simplified model (a) preliminary simplification (b) equivalent parameters simplification based on the Thevenin's theorem.

FIGURE 6. Geometric model of the rotor core outer-surface eccentric.

passes, can be calculated by:

$$\begin{cases} G_{2f,i} = \dfrac{\dfrac{\mu_0 \mu_{rf1} \Delta h_2 L_{ef}}{h_1} \cdot \dfrac{\mu_0 \mu_{rf2} \Delta h_{2f} L_{ef}}{n_x \Delta h_2}}{\dfrac{\mu_0 \mu_{rf1} \Delta h_2 L_{ef}}{h_1} + \dfrac{\mu_0 \mu_{rf2} \Delta h_{2f} L_{ef}}{n_x \Delta h_2}} & i \leq n_x \\ \dfrac{\mu_0 \mu_{rf2} \Delta h_{2f} L_{ef}}{(n_2 - n_x - 1)\Delta h_2} & i > n_x \end{cases} \quad (14)$$

where h_x is the height of the PMs in II region that the generated flux through the main magnetic flux direction; and

$$\Delta h_{2f} = \frac{t_{mb}}{2n_2} \quad (15)$$

$$n_x = round(\frac{h_x n_2}{h_2}) \quad (16)$$

where *round* is a function for towards nearest integer.

According to the Fig.5, the magnetic flux through the rotor yoke can be expressed by:

$$\varphi_{ry} = B_{sat} A_{ry} = \sum_{n_x+1}^{n_2} \varphi_{2,i} \frac{G_{2f,i}}{G_{2f,i} + G_{2,i}} \quad (17)$$

where B_{sat} is the flux density 2.1T, A_{ry} is $(R_{r5e}\text{-}R_{r6})L_{ef}$. Then n_x can be solved by the equation (17). Also, h_x can be estimated by the equation (16).

The model can be simplified as shown in Fig 5 (a). Equivalent flux φ_{pm1} and permeance G_{pm1} are calculated by:

$$\varphi_{pm1} = \sum_{i=1}^{n_1} \varphi_{1,i} \frac{G_{1f,i}}{G_{1f,i} + G_{1,i}} + \sum_{i=1}^{n_2} \varphi_{2,i} \frac{G_{2f,i}}{G_{2f,i} + G_{2,i}} \quad (18)$$

$$G_{pm1} = \sum_{i=1}^{n_1} \frac{G_{1,i} \cdot G_{1f,i}}{G_{1,i} + G_{1f,i}} + \sum_{i=1}^{n_2} \frac{G_{2,i} \cdot G_{2f,i}}{G_{2,i} + G_{2f,i}} + G_{mb1} + G_{mb2} \quad (19)$$

By the Thevenin's theorem, the EMCM can be further simplified as shown in Fig 5 (b). Equivalent external magnetomotive force, internal magnetic permeance and flux source can be calculated by:

$$F_{oc} = \frac{\varphi_{pm1}}{G_{pm1}} + \frac{\varphi_3}{G_3} + \frac{\varphi_4}{G_4} \quad (20)$$

$$G_{pme} = \frac{G_{pm1} \cdot G_3}{(2G_{pm1} + G_3)} \quad (21)$$

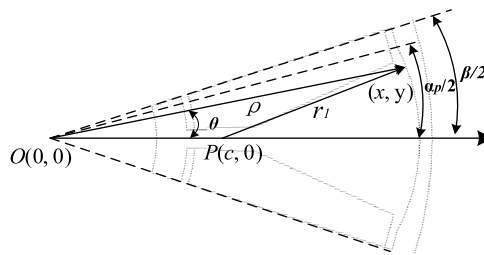$$\varphi_{pme} = F_{oc} \cdot G_{pme} \quad (22)$$

Therefore, average flux density on the rotor outer surface can be obtained by:

$$B_{reA} = \varphi_{pme} \frac{2G_{ge}}{(G_{ge} + 4G_{pme})A_m} \quad (23)$$

where A_m is the effectively magnetic flux area on the outer surface of the rotor.

If the EMCM is equivalent to the model that only a surface mount PM and air-gap region, then the equivalent parameters of PM remanence B_{reB} and thickness h_{pme} can be calculated by:

$$B_{reB} = \frac{\varphi_{pme}}{A_m} \quad (24)$$

$$h_{pme} = \frac{\mu_0 \mu_{rm} A_m}{2G_{pme}} \quad (25)$$

IV. AIR-GAP MAGNETIC FIELD ANALYSIS MODEL
A. ROTOR CORE ECCENTRIC STRUCTURE IN THE MODEL A
Based on the simplification of the rotor magnetic circuit above all, average magnetic density on the rotor outer surface has been obtained. As Fig 6 shows, point O (0, 0), namely origin coordinates, and P (c, 0) are the centers of the air-gap area and the surface of the rotor core, respectively. α_p is polar arc coefficient.

The scalar magnetic potential distribution in the air-gap regions is governed by Laplace's equation, i.e.

$$\frac{\partial^2 \Omega}{\partial r^2} + \frac{1}{r} \frac{\partial \Omega}{\partial r} + \frac{1}{r^2} \frac{\partial \Omega^2}{\partial \theta^2} = 0 \quad (26)$$

According to the periodicity of the field, the general solution in the air-gap regions can be expressed by:

$$\Omega(r, \theta) = \sum_{n=1}^{\infty} (A'_n r^{np} + B'_n r^{-np}) \cos np\theta \quad (27)$$

where Ω is related to the radial and circumferential components of $\vec{B}$ by:

$$\begin{cases} B_r = -\mu_0 \dfrac{\partial \Omega}{\partial r} \\ B_\theta = -\mu_0 \dfrac{1}{r} \dfrac{\partial \Omega}{\partial \theta} \end{cases} \quad (28)$$

The boundary conditions for the interfaces between air-gaps and stator core can be expressed by:

$$B_\theta(r, \theta)|_{r=R_{si}} = 0 \quad (29)$$

In the same way, under other coordinate that the point P $(c, 0)$ is used as the origin coordinates, the scalar magnetic potential distribution in the air-gap regions can be built by reference to (26), (27) and (28), then, the interfaces between air-gaps and the outer surface in the rotor can be expressed by:

$$B_{r1}(r, \theta) = -\mu_0 \frac{\partial \Omega}{\partial r_1} = B_{rotor} \qquad (30)$$

$$B_{rotor} = \sum_{m=1}^{\infty} \frac{4}{m\pi} B_{reA} \sin(\frac{m\pi\alpha}{2}) \qquad (31)$$

where r_1 is the arc radius of the surface of the rotor core, α is the angle with reference to d axis.

By combining (28) and (30), the radial density can be rewritten by:

$$B_r(r, \theta) = -\mu_0 \frac{\partial \Omega}{\partial r_1} \frac{\partial r_1}{\partial r} = B_{r1}(r, \theta) \frac{\partial r_1}{\partial r} \qquad (32)$$

From above boundary conditions (29), (27) can be simplified by:

$$B'_n = -A'_n R_{si}^{2np} \qquad (33)$$

From above boundary condition (30), whilst combined formula (31), (27) can be rewritten by:

$$\mu_0 \sum_{n=1}^{\infty} np(A'_n r^{np-1} - B'_n r^{-np-1}) \cos np\theta$$

$$= \frac{\partial r_1}{\partial r} \sum_{m=1}^{\infty} \frac{4}{m\pi} B_{reA} \sin(\frac{m\pi\alpha}{2}) \qquad (34)$$

when $n \neq m$,

$$A'_n r^{np-1} - B'_n r^{-np-1} = 0 \qquad (35)$$

then $A'_n = B'_n = 0$, which is contradictory with (27).

Therefore, only the equation $n = m$ is satisfied, (34) can be rewritten by:

$$-\mu_0 np(A'_n r^{np-1} - B'_n r^{-np-1}) = \frac{4}{n\pi} B_{reA} \sin(\frac{n\pi\alpha}{2}) \frac{\partial r_1}{\partial r} \qquad (36)$$

Assume that θ is the angular position referencing to in the rotor initial position; θ_{mp} is the angle with reference to the center of a nearest magnet pole. It can be calculated by:

$$\theta_{mp} = \begin{cases} \mod(\theta, \beta/2) & \text{if } k = even \\ \beta/2 - \mod(\theta, \beta/2) & elsewhere \end{cases} \qquad (37)$$

where β is the pole angle, i.e., $\beta = \pi/p$; k is the quotient that θ and $\beta/2$, i.e., $k = floor(\theta/(\beta/2))$; *floor* represents quotient function that take an integer down; *mod* represents remainder function.

Assume that the coordinate (x, y) represents the position of the outer surface of rotor core, where ρ is the distance to the point O.

$$(x - c)^2 + y^2 = r_1^2 \qquad (38)$$

Obviously, $x = \rho \cos \theta_{mp}, y = \rho \sin \theta_{mp}$; Substituting it to (38) can be obtained by:

$$r_1 = \sqrt{\rho^2 - 2\rho c \cos \theta_{mp} + c^2} \qquad (39)$$

The partial derivative of (39) is:

$$\frac{\partial r_1}{\partial \rho} = \frac{2\rho - 2c \cos \theta_{mp}}{2\sqrt{\rho^2 - 2\rho c \cos \theta_{mp} + c^2}} = \frac{\rho - c \cos \theta_{mp}}{r_1} \qquad (40)$$

Also, according to (39) and the geometric relationship as shown in Fig 6, variable ρ can be calculated by:

$$\rho(\theta) = \begin{cases} c \cos(\theta_{mp}) + \sqrt{r_1^2 - c^2 \sin^2 \theta_{mp}} \\ \qquad \text{if } 0 < \theta_{mp} \leq \frac{\alpha_p}{2} \\ \rho(\alpha_p/2) \quad \text{else } \frac{\alpha_p}{2} < \theta_{mp} \leq \frac{\beta}{2} \end{cases} \qquad (41)$$

where due to ρ is close to the distance r between air-gap region and point O, the equation $\frac{\partial r_1}{\partial r} \approx \frac{\partial r_1}{\partial \rho}$ is to be satisfied.

Therefore, according to (33) (36), coefficient A_n can be obtained by:

$$A_n = -\frac{\rho - c \cos \theta_{mp}}{\mu_0 np r_1} \frac{4}{n\pi} \frac{B_{reA} \sin(\frac{n\pi\alpha}{2})}{(\rho^{np-1} + R_{si}^{2np} \rho^{-np-1})} \qquad (42)$$

Based on (28) (33) and (42), the radial and circumferential components of the air-gap flux density can be obtained by:

$$B_r(r, \theta) = -\frac{\rho - c \cos \theta_{mp}}{r_1}$$
$$\cdot \sum_{n=1}^{\infty} \frac{4}{n\pi} \frac{B_{reA} \sin(\frac{n\pi\alpha}{2})}{((\frac{\rho}{R_{si}})^{np-1} + (\frac{R_{si}}{\rho})^{np+1})} ((\frac{r}{R_{si}})^{np-1}$$
$$+ (\frac{R_{si}}{r})^{np+1}) \cos np(\theta - \omega_r t) \qquad (43)$$

$$B_\theta(r, \theta) = \frac{\rho - c \cos \theta_{mp}}{r_1}$$
$$\cdot \sum_{n=1}^{\infty} \frac{4}{n\pi} \frac{B_{reA} \sin(\frac{n\pi\alpha}{2})}{((\frac{\rho}{R_{si}})^{np-1} + (\frac{R_{si}}{\rho})^{np+1})} ((\frac{r}{R_{si}})^{np-1}$$
$$- (\frac{R_{si}}{r})^{np+1}) \sin np(\theta - \omega_r t) \qquad (44)$$

B. EQUIVALENT MODEL BASED ON ONLY A SURFACE MOUNT PM AND AIR-GAP REGION IN THE MODEL B

According to the above EMCM in the model B, the equivalent parameters of PM remanence B_{reB} and thickness h_{pme} can be obtained as (24), (25), respectively. The radial and circumferential components of the air-gap flux density can be given by (45), (46), as shown at the top of the next page [30]–[32], where M_{rn}, $M_{\theta n}$ is the radial and tangential magnetization, respectively. when magnetization method of surface PM is parallel magnetization, then [16]

$$\begin{cases} M_{rn} = \frac{B_{reB}}{\mu_0} \alpha_p (A_{1n} + A_{2n}) \\ M_{\theta n} = \frac{B_{reB}}{\mu_0} \alpha_p (A_{1n} - A_{2n}) \end{cases} \qquad (47)$$

$$B_r(r,\theta) = \sum_{n=1}^{\infty} \frac{\mu_0}{\mu_{rm}}(M_{rn} + npM_{\theta n})\frac{np}{(np)^2-1}\left[\left(\frac{R_m}{r}\right)^{np+1} + \left(\frac{r}{R_s}\right)^{np-1}\left(\frac{R_m}{R_s}\right)^{np+1}\right]\cdot \cos np(\theta - \omega_r t)$$

$$\times \left\{ \frac{\left(np - \frac{1}{np}\right)\frac{M_{rn}}{M_{rn}+npM_{\theta n}} + \frac{1}{np} - 1 + 2\left(\frac{R_r}{R_m}\right)^{np+1} - \left[\left(np - \frac{1}{np}\right)\frac{M_{rn}}{M_{rn}+npM_{\theta p}} + \frac{1}{np} + 1\right]\left(\frac{R_r}{R_m}\right)^{2np}}{\frac{\mu_r+1}{\mu_r}\left[1 - \left(\frac{R_r}{R_s}\right)^{2np}\right] - \frac{\mu_r-1}{\mu_r}\left[\left(\frac{R_m}{R_s}\right)^{2np} - \left(\frac{R_r}{R_m}\right)^{2np}\right]} \right\} \quad (45)$$

$$B_\theta(r,\theta) = \sum_{n=1}^{\infty} \frac{\mu_0}{\mu_{rm}}(M_{rn} + npM_{\theta n})\frac{np}{(np)^2-1}\left[\left(\frac{R_m}{r}\right)^{np+1} - \left(\frac{r}{R_s}\right)^{np-1}\left(\frac{R_m}{R_s}\right)^{np+1}\right]\cdot \sin np(\theta - \omega_r t)$$

$$\times \left\{ \frac{\left(np - \frac{1}{np}\right)\frac{M_{rn}}{M_{rn}+npM_{\theta n}} + \frac{1}{np} - 1 + 2\left(\frac{R_r}{R_m}\right)^{np+1} - \left[\left(np - \frac{1}{np}\right)\frac{M_{rn}}{M_{rn}+npM_{\theta n}} + \frac{1}{np} + 1\right]\left(\frac{R_r}{R_m}\right)^{2np}}{\frac{\mu_r+1}{\mu_r}\left[1 - \left(\frac{R_r}{R_s}\right)^{2np}\right] - \frac{\mu_r-1}{\mu_r}\left[\left(\frac{R_m}{R_s}\right)^{2np} - \left(\frac{R_r}{R_m}\right)^{2np}\right]} \right\} \quad (46)$$

where

$$A_{1n} = \frac{\sin[(np+1)\alpha_p\frac{\pi}{2p}]}{(np+1)\alpha_p\frac{\pi}{2p}}$$

$$A_{1n} = 1 \quad \text{for } np = 1$$

$$A_{2n} = \frac{\sin[(np-1)\alpha_p\frac{\pi}{2p}]}{(np-1)\alpha_p\frac{\pi}{2p}} \quad \text{for } np \neq 1 \quad (48)$$

C. MAGNETIC FIELD DISTRIBUTION ON ARMATURE REACTION FIELD

Under load condition, the symmetric current excitations of phase a, b, and c as a Fourier series are given by:

$$\begin{cases} i_a = I_u \cos(p\omega_r t + \theta_u) \\ i_b = I_u \cos(p\omega_r t - 2\pi/3 + \theta_u) \\ i_c = I_u \cos(p\omega_r t + 2\pi/3 + \theta_u) \end{cases} \quad (49)$$

where θ_u is the harmonic phase angle, I_u is the current amplitude.

Therefore, the synthetic flux density in air-gap region excited by a symmetrical 3-phase winding current is obtained by [33]:

$$B_{rabc}(\theta, r, t)$$
$$= -\mu_0 \frac{2pI_u}{\pi}\frac{1}{r}\cdot \sum_{m=1}^{Q_s}(-1)^{floor(\frac{m}{2})}\cdot \sum_{n=1}^{\infty}K_{son}K_{pn}F_{nr}(r)$$
$$\times \cos(n(\theta - m\alpha_y) - p\omega_r t + \theta_u) \quad (50)$$

$$B_{\theta abc}(\theta, r, t)$$
$$= \mu_0 \frac{2pI_u}{\pi}\frac{1}{r}\cdot \sum_{m=1}^{Q_s}(-1)^{floor(\frac{m}{2})}\cdot \sum_{n=1}^{\infty}K_{son}K_{pn}F_{n\theta}(r)$$
$$\times \sin(n(\theta - m\alpha_y) - p\omega_r t + \theta_u) \quad (51)$$

where K_{son} is the slot-opening factor; K_{pn} is winding pitch factor; F_{nr} and $F_{n\theta}$ are two functions depend on the radius and harmonic order [24].

D. SLOTTED AIR-GAP FLUX DENSITY

The analytical method of the notion of complex relative air-gap permeance is adopted to calculate the magnetic field distribution in air-gap region with the effect of slotting. Refer to the documents [34], a complex number λ can be expressed by:

$$\lambda = \lambda_a + j\lambda_b \quad (52)$$

where

$$\begin{cases} \lambda_a = \lambda_0 + \sum_{n=1}^{\infty}\lambda_{an}\cos(nQ_s\theta) \\ \lambda_b = \sum_{n=1}^{\infty}\lambda_{bn}\sin(nQ_s\theta) \end{cases} \quad (53)$$

where the Fourier coefficients λ_{an} and λ_{bn} can be calculated by using discrete Fourier transform.

Therefore, the radial and tangential components of the flux density in the slotted air-gap can be calculated by [35]:

$$\begin{cases} B_{sr} = B_r\lambda_a + B_\theta\lambda_b \\ B_{s\theta} = B_\theta\lambda_a - B_r\lambda_b \end{cases} \quad (54)$$

$$\begin{cases} B_{srabc} = B_{rabc}\lambda_a + B_{\theta abc}\lambda_b \\ B_{s\theta abc} = B_{\theta abc}\lambda_a - B_{rabc}\lambda_b \end{cases} \quad (55)$$

E. ELECTROMAGNETIC PERFORMANCE

The flux linkage of single tooth can be calculated by:

$$\Phi_i(t) = N_c R_g L_{ef}\int_{\alpha_i-\tau/2}^{\alpha_i+\tau/2}(B_{sr}(\theta,t) + B_{sabcr}(\theta,t))d\theta \quad (56)$$

where α_i is the angle of stator axis, τ is coil pitch for one coil of any phase. The total phase flux linkage can be calculated by summing the phase winding flux linkage in corresponding stator. For 10-pole/12-slot, any phase flux linkage can be expressed by:

$$\Phi_k = \Phi_i - \Phi_{i+1} - (\Phi_{i+Q_s/2} - \Phi_{i+Q_s/2+1}) \quad (57)$$

where k represents phase a, b and c, respectively.

TABLE 2. Main specifications parameters of the two structure rotors.

Symbol	Quantity	Value and unit	
		Model A	Model B
R_{r1}	Radius of the rotor outer surface	24.2 mm	24.2 mm
R_{r2}	Radius of the rotor core outer surface	23.64 mm	22.7 mm
R_{r3}	Radius of the spoke PM outer surface	23.27mm	22.35mm
R_{r4}	Radius of the spoke PM inner surface	9 mm	9.5 mm
R_{r6}	Radius of the shaft	7 mm	7 mm
t_{mb}	Width of magnetic bridge	1 mm	1 mm

Thus, the back-EMF can be obtained as:

$$E_a = -\frac{d\Phi_a}{dt} \tag{58}$$

$$T_e = \frac{L_{ef} r^2}{\mu_0} \int_0^{2\pi} B_{sr}(\theta, r, t) \cdot B_{s\theta abc}(\theta, r, t) \\ + B_{s\theta}(\theta, r, t) \cdot B_{srabc}(\theta, r, t) d\theta \tag{59}$$

V. ANALYTICAL PREDICTION AND VERIFICATION BY FEA

In this section, the proposed two models will be validated by 10-pole/12-slot compared with the results of the FEA. To order to obtain an accurate electromagnetic performance, the total number of nodes in the motor with the spoke-Type rotor and hybrid rotor structure are 18429 and 23113 in 2-D FEA, respectively. The stator core B-H curve with a nonlinear change has a knee point of 1.7T. The torque will be verified when the current amplitude is 50A with the stator unsaturated. Their main parameters of the rotor are given in Table 2.
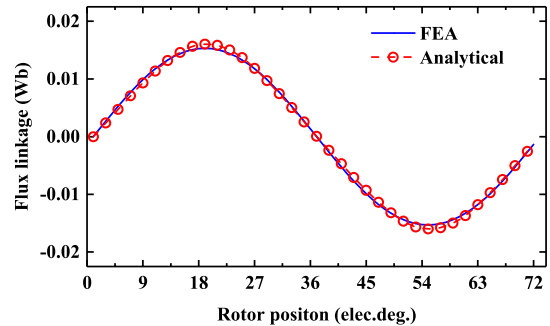
A. THE MODEL A VALIDATION

Based on the above parameters in Model A, the flux density components in middle air-gap region between FEA and analytical model are shown in Fig 7 (a) and (b), respectively. Fig 8 and Fig 9 are for the flux linkage and back-EMF, respectively. The electromagnetic torque is shown in Fig 10.

All analytical electromagnetic performances show a good agreement with FEA relatively. However, there is a difference between FEA and analytical model in circled area as shown in Fig 7. This is because that the flux density of the rotor core is not actually evenly distributed to the rotor outer surface in FEA, which is not in accordance with the assumptions in analytical predictions. Furthermore, the error of the circumferential flux density has been more impacted on the performance prediction than the radius flux density. In actual, the radius flux density is more significant influence to predict the flux linkages and back-EMF at the first stage of the design process. From the Fig 8 and Fig 9, it can be seen that the amplitude of the flux linkages and the back-EMF show good well agreement. The average torque is 5.98N.m in analytical model compared with the average torque is 6.04N.m in FEA when the peak current is 50A in the control mode of $I_d = 0$. The accuracy of prediction with about 1.0% is excellent although the predicted performance of torque ripples shows larger errors as shown in Table 3.
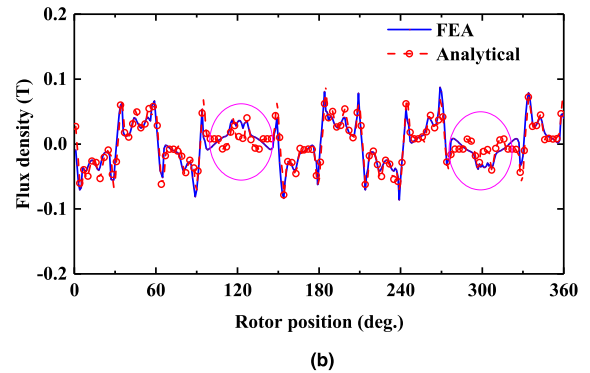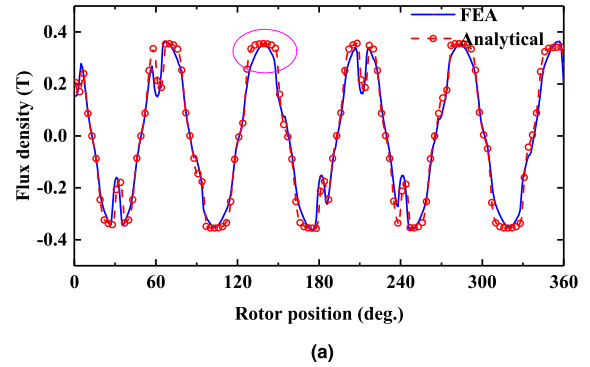
FIGURE 7. No-load air-gap flux density waveforms by the FEA and analytical prediction of the model A (a) radial component (b) circumferential component.

FIGURE 8. The flux linkage under no-load condition.
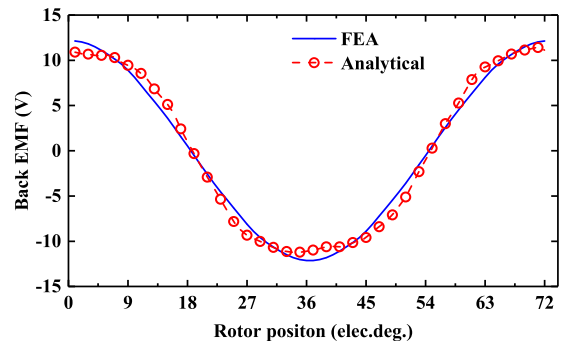
FIGURE 9. The back-EMF under no-load condition.

B. THE MODEL B VALIDATION

Based on the above parameters of the Table 2 in Model B, the air-gap flux density components between FEA and analytical
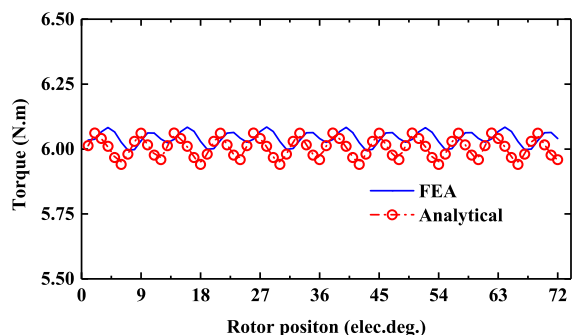
FIGURE 10. Variation of torque with electrical angle when the current I_u = 50A.
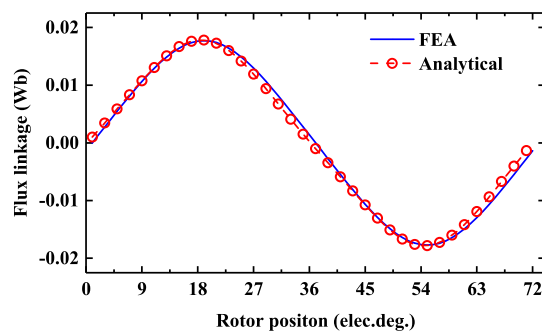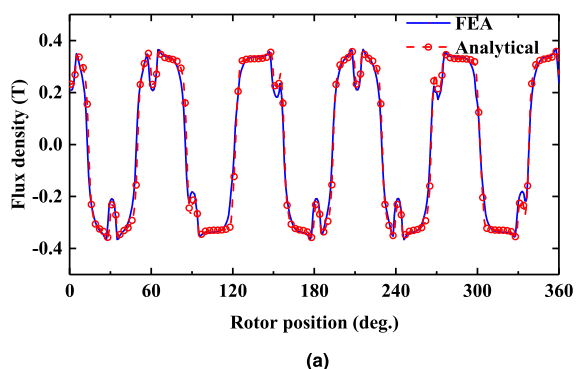

(a)

(b)

FIGURE 11. No-load air-gap flux density waveforms by the FEA and analytical prediction of the model B (a) radial component (b) circumferential component.

FIGURE 12. The flux linkage under no-load condition.

FIGURE 13. The back-EMF under no-load condition.
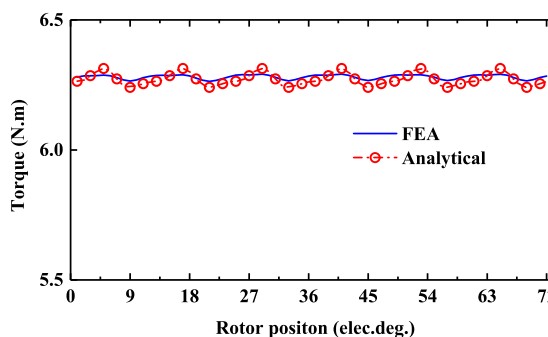
FIGURE 14. Variation of torque with electrical angle when the current I_u = 50A.

model are shown in Fig 11 (a) and (b), respectively. Fig 12 and Fig 13 are for the flux linkage and back-EMF, respectively. Fig 14 is for the electromagnetic torque. The waveforms of the electromagnetic performance show high accuracy with comparison between the FEA and analytical model.

As shown in Fig 11, the comparisons in the model B show a smaller error of the air-gap flux density between the FEA and analytical model than the errors in the model A. It is well worth to be noted that: the air-gap region is in direct contact with the surface-mount PMs in hybrid structure rotor, then the air-gap flux density can be little impacted by the rotor iron outer-surface with uneven flux density distribution as the model A. Therefore, not only the torque amplitude can be predicted very well with the error of 0.5%, excellent
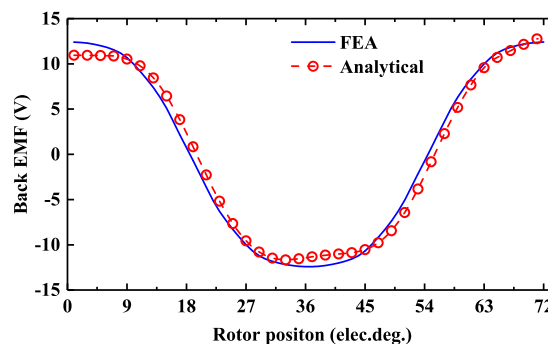
agreement between the predictions of torque ripples can be achieved as shown in Fig 14 with the same control current and control mode.

C. COMPARISONS OF THE MAGNETIC PERFORMANCE BETWEEN TWO MODELS

The comparisons of the average torque and torque ripples are shown in Table 3. It is obvious that the torque of STR is relatively larger than that of HRS in the FEA and analytical model. The reason is that the thickness of the PMs at the main flux path is increased, even though there is a little reduction in width of the spoke-type PMs because of the restriction of the rotor size. The fundamental amplitude i.e. 5th harmonic of the air-gap flux density is higher in the HRS than in the STR as shown in Fig 15. Therefore, the torque density can be

TABLE 3. The comparisons of the average torque and torque ripples.

method	torque (STR)	torque (HRS)	Torque ripple (STR)	Torque ripple (HRS)
FEA	6.04	6.28	1.3%	0.9%
Analytical	5.98	6.27	3.6%	1.1%
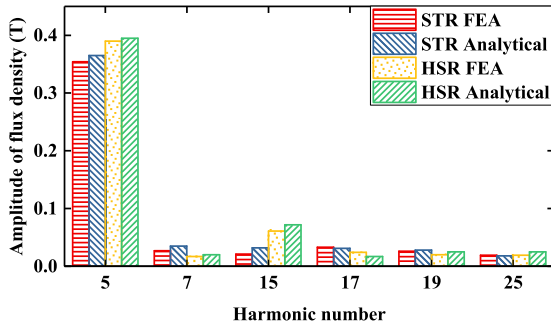
FIGURE 15. Harmonic component of STR and HRS model predicted by the flux density between the FEA and analytical model.

increased by adopting the proposed model of the hybrid rotor structure (HRS).

Moreover, the torque ripples have smaller values whether it is in the FEA or analytical model, which can exclude the influence of the calculation error with uneven flux density distribution in the rotor iron outer-surface of the model A. According to the aforementioned, the surface mount PMs in HRS, which magnetic permeability is close to 1, is equivalent to increase the effective length of the air-gap. Then, the effects of the slotted opening are weakened. The ratio of the inter-harmonics contents decreases such as 7th, 17th, and 19th, as shown in Fig 15. This is not to be considered in ripples that 15th harmonic which is three times the fundamental does not react with the armature.

The FEA and analytical model has its own advantage and application. The FEA is suitable for accurate calculation of the flux density, back-EMF and torque, even considering the effects of saturation and demagnetization. However, this is the exchanged result at the expense of time compared with the analytical model. The computation times of the two methods in the model A is 143.5s and 27.7s, respectively. Correspondingly, the times in the model B is 177.6s and 32.6s, respectively. It is demonstrated that the analytical model can save nearly 80.7% and 81.7% of the simulation time compared with the FEA, respectively. It is very significant to optimize solutions at the initial design process.

VI. CONCLUSION

In this paper, two analytical methods have been proposed to predict the magnetic field distribution and the torque performance in the machines with the irregular rotor structure. The equivalent magnetic network model has been established considering leakage flux linkage and irregular PM shape. In order to obtain boundary conditions in the model with the STR and HRS, two equivalent methods have been adopted:

one is that the average flux density in the rotor core outer surface is obtained as the boundary conditions of Laplace's equation in the air-gap regions of model A; The other is that the equivalent parameters of PM remanence B_{reB} and thickness h_{pme} can be obtained by the Thevenin's theorem in the model B.

Based on the boundary conditions, the magnetic field analysis result has been obtained with considering for the rotor core outer-surface eccentric in the model A. Meanwhile, by utilizing the equivalent parameters of B_{reB} and h_{pme}, the air-gap magnetic density has been solved for conventional classic magnetic field analysis model of surface-mounted PMs with air-gap in model B. To validate the good accuracy for the air-gap density component, flux linkage, back-EMF, and torque, the respective comparison results between the FEA and the analytical model have been shown, which revealed that results can match well with each other. Then the analytical model can save nearly 80% computation time. In addition, the machine with the proposed hybrid PM rotor structure can improve the torque density compared with that of the spoke-type PM structure rotor.

REFERENCES

[1] G. Xu, G. Liu, W. Zhao, Q. Chen, and X. Du, "Principle of torque-angle approaching in a hybrid rotor permanent-magnet motor," *IEEE Trans. Ind. Electron.*, vol. 66, no. 4, pp. 2580–2591, Apr. 2019.

[2] Y. Fan, W. Zhu, X. Zhang, M. Cheng, and K. T. Chau, "Research on a single phase-loss fault-tolerant control strategy for a new flux-modulated permanent-magnet compact in-wheel motor," *IEEE Trans. Energy Convers.*, vol. 31, no. 2, pp. 658–666, Jun. 2016.

[3] G. Liu, L. Liu, Q. Chen, and W. Zhao, "Torque calculation of five-phase interior permanent magnet machine using improved analytical method," *IEEE Trans. Energy Convers.*, vol. 34, no. 2, pp. 1023–1032, Jun. 2019.

[4] Q. Chen, G. Xu, G. Liu, W. Zhao, Z. Lin, and L. Liu, "Torque ripple reduction in five-phase IPM motors by lowering interactional MMF," *IEEE Trans. Ind. Electron.*, vol. 65, no. 11, pp. 8520–8531, Nov. 2018.

[5] A. M. El-Refaie, "Fractional-slot concentrated-windings synchronous permanent magnet machines: Opportunities and challenges," *IEEE Trans. Ind. Electron.*, vol. 57, no. 1, pp. 107–121, Jan. 2010.

[6] X. Ge, Z. Q. Zhu, J. B. Li, and J. T. Chen, "A spoke-type IPM machine with novel alternate airspace barriers and reduction of unipolar leakage flux by step-staggered rotor," in *Proc. IEEE Int. Electr. Mach. Drives Conf.*, May 2016, pp. 53–59.

[7] P. Liang, F. Chai, Y. Yu, and L. Chen, "Analytical model of a spoke-type permanent magnet synchronous in-wheel motor with trapezoid magnet accounting for tooth saturation," *IEEE Trans. Ind. Electron.*, vol. 66, no. 2, pp. 1162–1171, Feb. 2019.

[8] S.-I. Kim, J. Cho, S. Park, T. Park, and S. Lim, "Characteristics comparison of a conventional and modified spoke-type ferrite magnet motor for traction drives of low-speed electric vehicles," *IEEE Trans. Ind. Appl.*, vol. 49, no. 6, pp. 2516–2523, Nov. 2013.

[9] S. Kim, S. Park, T. Park, J. Cho, W. Kim, and S. Lim, "Investigation and experimental verification of a novel spoke-type ferrite-magnet motor for electric-vehicle traction drive applications," *IEEE Trans. Ind. Electron.*, vol. 61, no. 10, pp. 5763–5770, Oct. 2014.

[10] W. Kakihara, M. Takemoto, and S. Ogasawara, "Rotor structure in 50 kW spoke-type interior permanent magnet synchronous motor with ferrite permanent magnets for automotive applications," in *Proc. IEEE Energy Convers. Congr. Expo.*, Sep. 2013, pp. 606–613.

[11] M.-J. Kim, S.-Y. Cho, K.-D. Lee, J.-J. Lee, J.-H. Han, T.-C. Jeong, W.-H. Kim, D.-H. Koo, and J. Lee, "Torque density elevation in concentrated winding interior PM synchronous motor with minimized magnet volume," *IEEE Trans. Magn.*, vol. 49, no. 7, pp. 3334–3337, Jul. 2013.

[12] J. Li, K. Wang, and C. Liu, "Comparative study of consequent-pole and hybrid-pole permanent magnet machines," *IEEE Trans. Energy Convers.*, vol. 34, no. 2, pp. 701–711, Jun. 2019.

[13] K. Wang, J. Li, S. S. Zhu, and C. Liu, "Novel hybrid-pole rotors for consequent-pole PM machines without unipolar leakage flux," *IEEE Trans. Ind. Electron.*, vol. 66, no. 9, pp. 6811–6823, Sep. 2019.

[14] L. J. Wu and Z. Q. Zhu, "Simplified analytical model and investigation of open-circuit ac winding loss of permanent-magnet machines," *IEEE Trans. Ind. Electron.*, vol. 61, no. 9, pp. 4990–4999, Sep. 2014.

[15] L. J. Wu, Z. Q. Zhu, D. Staton, M. Popescu, and D. Hawkins, "Sub-domain model for predicting armature reaction field of surface-mounted permanent-magnet machines accounting for tooth-tips," *IEEE Trans. Magn.*, vol. 47, no. 4, pp. 812–822, Apr. 2011.

[16] Z. Q. Zhu, D. Howe, and C. C. Chan, "Improved analytical model for predicting the magnetic field distribution in brushless permanent-magnet machines," *IEEE Trans. Magn.*, vol. 38, no. 1, pp. 229–238, Aug. 2002.

[17] X. Chen, J. Hu, K. Chen, and Z. Peng, "Modeling of electromagnetic torque considering saturation and magnetic field harmonics in permanent magnet synchronous motor for HEV," *Simul. Model. Pract. Theory*, vol. 66, pp. 212–225, Aug. 2016.

[18] L. J. Wu, Z. Q. Zhu, D. Staton, M. Popescu, and D. Hawkins, "Analytical model for predicting magnet loss of surface-mounted permanent magnet machines accounting for slotting effect and load," *IEEE Trans. Magn.*, vol. 48, no. 1, pp. 107–117, Jan. 2012.

[19] Y. Oner, Z. Q. Zhu, L. J. Wu, X. Ge, H. Zhan, and J. T. Chen, "Analytical on-load subdomain field model of permanent-magnet Vernier machines," *IEEE Trans. Ind. Electron.*, vol. 63, no. 7, pp. 4105–4117, Jul. 2016.

[20] L. Roubache, K. Boughrara, F. Dubas, and R. Ibtiouen, "New subdomain technique for electromagnetic performances calculation in radial-flux electrical machines considering finite soft-magnetic material permeability," *IEEE Trans. Magn.*, vol. 54, no. 4, Apr. 2018, Art. no. 8103315.

[21] M. Pourahmadi-Nakhli, A. Rahideh, and M. Mardaneh, "Analytical 2-D model of slotted brushless machines with cubic spoke-type permanent magnets," *IEEE Trans. Energy Convers.*, vol. 33, no. 1, pp. 373–382, Mar. 2018.

[22] Y. Zhou, H. Li, G. Meng, S. Zhou, and Q. Cao, "Analytical calculation of magnetic field and cogging torque in surface-mounted permanent-magnet machines accounting for any eccentric rotor shape," *IEEE Trans. Ind. Electron.*, vol. 62, no. 6, pp. 3438–3447, Jun. 2015.

[23] G. Liu, G. Xu, W. Zhao, X. Du, and Q. Chen, "Improvement of torque capability of permanent-magnet motor by using hybrid rotor configuration," *IEEE Trans. Energy Convers.*, vol. 32, no. 3, pp. 953–962, Sep. 2017.

[24] L. J. Wu, Z. Li, X. Huang, Y. Zhong, Y. Fang, and Z. Q. Zhu, "A hybrid field model for open-circuit field prediction in surface-mounted PM machines considering saturation," *IEEE Trans. Magn.*, vol. 54, no. 6, Jun. 2018, Art. no. 8103812.

[25] P. Liang, F. Chai, Y. Bi, Y. Pei, and S. Cheng, "Analytical model and design of spoke-type permanent-magnet machines accounting for saturation and nonlinearity of magnetic bridges," *J. Magn. Magn. Mater.*, vol. 417, pp. 389–396, Nov. 2016.

[26] A. Hanic, D. Zarko, D. Kuhinek, and Z. Hanic, "On-load analysis of saturated surface permanent magnet machines using conformal mapping and magnetic equivalent circuits," *IEEE Trans. Energy Convers.*, vol. 33, no. 3, pp. 915–924, Sep. 2018.

[27] A. Hanic, D. Zarko, and Z. Hanic, "A novel method for no-load magnetic field analysis of saturated surface permanent-magnet machines using conformal mapping and magnetic equivalent circuits," *IEEE Trans. Energy Convers.*, vol. 31, no. 2, pp. 740–749, Jun. 2016.

[28] K. Abbaszadeh and F. R. Alam, "On-load field component separation in surface-mounted permanent-magnet motors using an improved conformal mapping method," *IEEE Trans. Magn.*, vol. 52, no. 2, 2015.

[29] L. Zhu, S. Z. Jiang, Z. Q. Zhu, and C. C. Chan, "Analytical modeling of open-circuit air-gap field distributions in multisegment and multilayer interior permanent-magnet machines," *IEEE Trans. Magn.*, vol. 45, no. 8, pp. 3121–3130, Aug. 2009.

[30] Z. Q. Zhu, D. Howe, and E. Bolte, "Instantaneous magnetic field distribution in brushless permanent magnet DC motors, Part I: Open-circuit field," *IEEE Trans. Magn.*, vol. 29, no. 1, pp. 124–135, Jan. 1993.

[31] S. T. Boroujeni, P. Jalali, and N. Bianchi, "Analytical modeling of no-load eccentric slotted surface-mounted PM machines: Cogging torque and radial force," *IEEE Trans. Magn.*, vol. 53, no. 12, Dec. 2017, Art. no. 8113008.

[32] S. G. Min and B. Sarlioglu, "Fast and systematic design optimization of surface-mounted PM machines using advanced analytical models and subharmonic elimination methods," *IEEE Trans. Magn.*, vol. 55, no. 1, Jan. 2019, Art. no. 8100216.

[33] Z. Q. Zhu and D. Howe, "Instantaneous magnetic field distribution in brushless permanent magnet DC motors Part 11: Armature-reaction field," *IEEE Trans. Magn.*, vol. 29, no. 1, pp. 136–142, Jan. 1993.

[34] D. Zarko, D. Ban, and T. A. Lipo, "Analytical calculation of magnetic field distribution in the slotted air gap of a surface permanent-magnet motor using complex relative air-gap permeance," *IEEE Trans. Magn.*, vol. 42, no. 7, pp. 1828–1837, Jul. 2006.

[35] Z. Q. Zhu and D. Howe, "Instantaneous magnetic field distribution in permanent magnet brushless DC motors. IV. Magnetic field on load," *IEEE Trans. Magn.*, vol. 29, no. 1, pp. 152–158, Jan. 1993.

YU-XI LIU was born in Hunan, China. He received the B.E. and M.E. degrees in electrical engineering from Xi'an High-Tech Institution, Xi'an, China, in 2014 and 2017, respectively. He is currently pursuing the Ph.D. degree with the School of the Xi'an High-Tech Institution.

He is the Co-Cultivation Doctor of the Harbin Institute of Technology. His current research interest includes design of high-power/torque density permanent magnetic machines.

LI-YI LI (M'09–SM'17) received the B.E., M.E., and D.E. degrees from the Harbin Institute of Technology (HIT), Harbin, China, in 1991, 1995, and 2001, respectively.

In 2013, he became "Yangtze Fund Scholar" a Distinguished Professor and is currently supported by the National Science Fund for Distinguished Young Scholars. Since 2004, he has been a Professor with the School of Electrical Engineering and Automation, HIT. He has authored or coauthored more than 110 technical papers and is the holder of 50 patents. His research interests include design, drive, and control of linear motors, and design and drive of high-speed/power density permanent magnet machines.
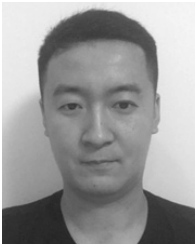
QIN-HE GAO received the B.E., M.E., and D.E. degrees from Xi'an High-Tech Institution, Xi'an, China, in 1989, 1993, and 2002, respectively.

Since 2010, he has been a Professor with the School of the Institute of Armament Science and Technology, Xi'an High-Tech Institution. His research interests include electro-hydraulic system simulation and electromechanical control technology.

JI-WEI CAO received the B.E. and M.E. degrees in electrical engineering from the Shenyang University of Technology (SUT), Shenyang, China, in 2005 and 2008, respectively, and the D.E. degree in electrical engineering from the Harbin Institute of Technology (HIT), Harbin, China, in 2014, where he is currently with the Institute of Electromagnetic and Electronic Technology.

His research areas include the development and improvement of power density for the effective design of electric motor.

ZHI-YIN SUN (M'17) received the B.E., M.E., and D.E. degrees in electrical engineering from the Harbin Institute of Technology (HIT), in 2009, 2011, and 2016, respectively.

She was a joint Training Doctoral Student with Physikalisch-Technische Bundesanstalt, Germany, from 2014 to 2015, working on precise magnetic field analysis. She is currently a Research Associate with the Laboratory for Space Environment and Physical Sciences, HIT. She is also a Postdoctoral with the Helmholtz-Institute Mainz, Germany. Her research interests include electrical machines, weak magnetic field realization, and ultra-sensitive measurement.

Dr. Sun is awarded a scholarship under the International Postdoctoral Exchange Fellowship Program 2017.

REN-HAO WANG received the B.E. degree from Xi'an High-Tech Institution, Xi'an, China, in 2014.

He is currently a Research Associate with the Product Inspection Laboratory, Harbin Representative Office, which is responsible for product acceptance of the Harbin Institute of Technology. His research interest includes the development of mechanical design.

• • •